OPEN

Enhanced multiple vibrational resonances by Na$^+$ and K$^+$ dynamics in a neuron model

Xing-Xing Wu[1], Chenggui Yao[1,2] & Jianwei Shuai[1]

[1]Department of Physics, Xiamen University, Xiamen 361005, China, [2]Department of Mathematics, Shaoxing University, Shaoxing 312000, China.

Some neuronal receptors perceive external input in the form of hybrid periodic signals. The signal detection may be based on the mechanism of vibrational resonance, in which a system's response to the low frequency signal can become optimal by an appropriate choice of the vibration amplitude of HFS. The vibrational resonance effect is investigated in a neuron model in which the intra- and extra-cellular potassium and sodium concentrations are allowed to evolve temporally, depending on ion currents, Na$^+$-K$^+$ pumps, glial buffering, and ion diffusion. Our results reveal that, compared to the vibrational resonances in the model with constant ion concentrations, the significantly enhanced vibrational multi-resonances can be observed for the single neuron system where the potassium and sodium ion concentrations vary temporally. Thus, in contradiction to a popular view that ion concentrations dynamics play little role in signal detection, we indicate that the neuron's response to an external subthreshold signal can be largely improved by sodium and potassium dynamics.

Two-frequency periodic signals are pervasive and significant in many science and application fields[1–5], especially in biology fields. Many animals perceive external input from their surroundings in the form of hybrid signals with multiple frequencies. One of the well studied examples is weakly electric fish which are both electrogenic and electro-receptive. When they are in the vicinity of one another, they communicate through electric organ discharges with a frequency range of 500–700 Hz for females and 800–1000 Hz for males. These signals, together with low frequency signals (<20 Hz) from environmental information, would be sensed by electroreceptors in the fish's skin and used for navigation, electrocommunication and electrolocation[6].

Now comes an interesting question of how animals such as weakly electric fish manage to get useful information from the input of hybrid signals. To be specific, how do the neurons of weakly electric fish decipher the low frequency signals from the high frequency modulated signals? Middleton et. al have discussed the cellular basis for the parallel transmission of two signals of different frequencies in an electrosensory system[7], envelope encoding and lower frequency signal extraction in a sensory pathway[8,9]. Electric images of one fish in the company of another one at three representative phases within a beat cycle have also been discussed[10]. Moreover, the processing of two stimulus attributes by midbrain electrosensory neurons have been studied[11].

Besides electric organ discharges, it has also been discovered that two frequency bands are significant for long distance vocal communication in the green treefrog[12] and that applying electrical stimulation with different frequencies to certain body cites facilitates the release of specific neuropeptides in the central nervous system[13]. The visual evoked potentials with stimuli modulated by sinusoids at distinct frequencies have been studied by Victor et. al[14].

The mechanism for hybrid signal detection may depend on the principle of vibrational resonance (VR), when a system' s response to a low-frequency signal (LFS) can become optimal by an appropriate choice of the vibration amplitude of the high-frequency signal (HFS)[15]. This phenomenon is similar to the stochastic resonance, where random noise enhances the response at the frequency of a subthreshold signal[16–18]. Due to the significance of its potential application, the VR phenomenon has already been studied numerically, analytically or experimentally[19–26].

Previous investigations into the applications of VR to neuroscience are mostly based on too simplified neuron models, such as FHN model[20,24,27,28]. Instead, we adopt a multi-compartment neuron model with five types of active ionic channels. It has been revealed that this model can present rich dynamical phenomena and exhibit several firing patterns when stimulated by various depolarizing DC current intensity[29]. The

model later was modified to allow potassium accumulation in an interstitial space outside the cell[30]. To make it more biologically realistic, we further improve the model by allowing potassium and sodium concentrations inside the cell and in the interstitial space to evolve dynamically.

We are curious about the effect of ion concentrations dynamics on VR, although they are not considered important in signal detection for neuron systems in previous simulations. The variation in ion concentrations not only depends on but also affects the electrical behavior of individual neurons. During neuronal activity ions move across the membrane, causing variation in ion concentrations, especially the increase in extracellular potassium ($[K^+]_o$) and intracellular sodium concentrations ($[Na^+]_i$). Neurons are tightly packed in mammalian brains resulting in small intra- and extra-cellular volumes. Thus, ion concentrations dynamics should have a large effect on neuron activity.

Actually, it has been recognized long ago that potassium accumulation occurs during neuronal firing[31–33] and that sodium concentrations alter due to variation in membrane potential[34,35]. In addition, it has been proposed that abnormal potassium concentration plays a key role in some pathological states of the central nervous system, such as hypoxia induced spreading depression[36] and in diseases including diabetes and arrhythmias[37–40]. Besides, it has been suggested that epilepsy is connected with a reduction of the $Na^+ - K^+$ pump[41] and impairment of the glial K^+ uptake[42], and it has been reported that extracellular K^+ concentration has effects on firing patterns of low calcium epileptiform activity[43–45]. Recently, computer simulations have pointed out the critical roles of variable ion concentrations. It was suggested that dynamical ion concentrations are responsible for some particular physiological electrical oscillations, and that proper neuronal function requires ion concentration homeostasis[46–48]. The changes of $[K^+]_o$ can modulate bursting frequency and cause multi-stability[49,50]. It has also been suggested that K^+ diffusion among neighboring cells is a contributing factor in the establishment of periodic neuronal firing in a small network[30,51].

In this paper, we use a biophysically plausible neuron model with sodium and potassium dynamics to investigate its responses to external biharmonic signals. We find that, although the multiple VRs can be observed in the model with constant ion concentrations, the presence of temporally dynamical ion concentrations significantly broadens the VRs when the two signals have much different signals.

The contents of this paper are organized as follows: The neuron model subject to a LFS and a high frequency driving force is introduced in Sec. II. The full model is formulated for which ion concentrations are dynamically dependent on the competition of ion currents, $Na^+ - K^+$ pumps, glial buffering, and ion diffusion. To understand the role of ion concentrations dynamics in signal detection, we make the ion concentrations stay at their equilibrium levels to formulate a reduction of this model to make comparisons. In Sec. III, It is observed that VRs are induced by adjusting the amplitude of the high-frequency force for these two models. The different results by these two models are compared and the effects of ion concentration dynamics on VRs are addressed. Finally, conclusions are made in Sec. IV.

Formulism

The neuron model is schematically shown in Fig. 1. The neuron comprises ten compartments of apical dendrites, five compartments of basal dendrites, and a soma compartment. All active ionic channels are assumed to be included in the soma. The extracellular space outside the soma separates into an interstitial space immediately surrounding the soma and the bath.

Membrane potential dynamics. The ordinary differential equations governing the membrane potential are as follows:

$$C_s \frac{dV_s}{dt} = -\left(I_{Na} + I_K + I_{sLeak} + I_{pump} + I_{sd}\right) + I_{stim}$$
$$I_{stim} = A\cos(\omega t) + B\cos(N\omega t) \tag{1}$$

$$C_d \frac{dV_{d,n}}{dt} = -\left(I_{dLeak,n} + I_{dd,n}\right), \tag{2}$$

where $0 \le n \le 15$ and $n \ne 5$. V_s is the membrane potential for the somatic compartment and $V_{d,n}$ for the dendritic compartments. The stimulus current I_{stim} applied to the soma has an external LFS $A\cos(\omega t)$ and an external HFS $B\cos(N\omega t)$. Note that the angular frequency of the high-frequency force is N times higher than that of the LFS.

Relevant somatic currents include the sum of Na^+ currents I_{Na}, the sum of K^+ currents I_K, the leakage current I_{sLeak}, the current caused by the Na^+-K^+ pump I_{pump} and the axial current I_{sd}. Specifically, somatic currents are given by

$$
\begin{aligned}
I_{Na} &= I_{NaF} + I_{NaP} + I_{NaLeak} \\
I_{NaF} &= g_{NaF} m^3 h (V_s - E_{Na}) \\
I_{NaP} &= g_{NaP} w (V_s - E_{Na}) \\
I_{NaLeak} &= g_{NaLeak} (V_s - E_{Na}) \\
I_K &= I_{KDR} + I_{KA} + I_{KM} + I_{KLeak} \\
I_{KDR} &= g_{KDR} n^4 (V_s - E_K) \\
I_{KA} &= g_{KA} a b (V_s - E_K) \\
I_{KM} &= g_{KM} u^2 (V_s - E_K) \\
I_{KLeak} &= g_{KLeak} (V_s - E_K) \\
I_{sLeak} &= g_{sLeak} (V_s - E_{sLeak}) \\
I_{pump} &= I_{max} \left(1 + \frac{3.5}{[K^+]_o}\right)^{-2} \left(1 + \frac{10}{[Na^+]_i}\right)^{-3} \\
I_{sd} &= g_{5,4} (V_s - V_4) + g_{5,6} (V_s - V_6),
\end{aligned}
\tag{3}
$$

where

$$E_K = 26.71 \times \ln\left(\frac{[K^+]_o}{[K^+]_i}\right)$$

$$E_{Na} = 26.71 \times \ln\left(\frac{[Na^+]_o}{[Na^+]_i}\right)$$

which both have the unit of mV and vary with time. The active pump is implemented for the balance of sodium and potassium ions and it is electrogenic because more sodium is extruded than potassium absorbed[47].

The currents through the voltage-dependent channels are controlled by the gating variables m, h, w, n, a, b, and u. These activation and inactivation variables represent probabilities of ion channels that are in the open state. They vary between 0 and 1 and obey the form:

$$\frac{dx}{dt} = \frac{x_\infty(V) - x}{\tau_x} = \alpha_x(V) - x(\alpha_x(V) + \beta_x(V)), \tag{4}$$

where x represents m, h, w, n, a, b, and u.

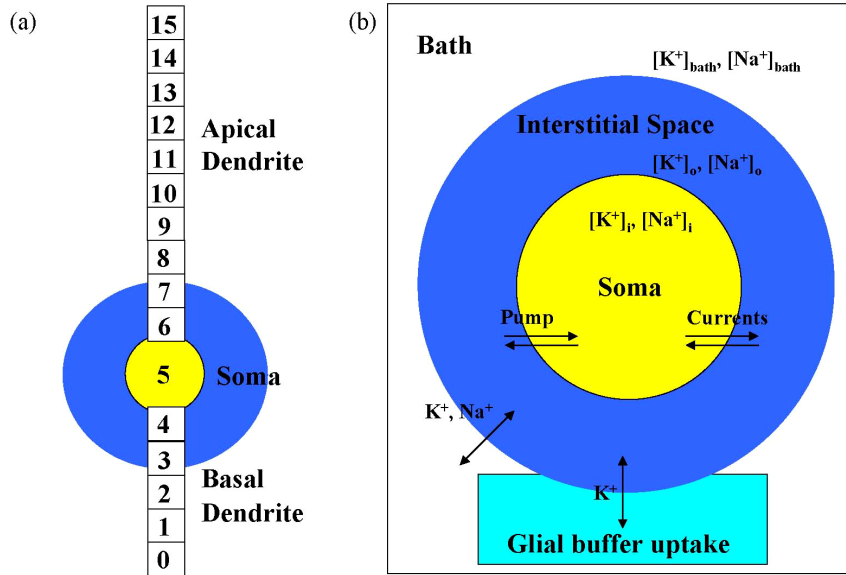For dendrite compartments, the currents are given by

Figure 1 | Schematic diagram of the neuron model. (a) This neuron comprises ten compartments of apical dendrites, five compartments of basal dendrites, and a soma compartment. (b) Ion concentrations inside (yellow area) and outside (blue shell) the soma of the cell are regulated by ionic currents, the Na$^+$-K$^+$ exchange pump, glial buffering, and ion diffusion between the interstitial space and the bath.

$$I_{\text{dLeak},n} = g_{\text{dLeak}}(V_n - E_{\text{dLeak}})$$
$$I_{\text{dd},n} = g_{n,n-1}(V_{\text{d},n} - V_{n-1}) + g_{n,n+1}(V_{\text{d},n} - V_{n+1}), \qquad (5)$$

where $I_{\text{dd},n}$ is the axial current caused by the potential difference between neighboring dendrite sections. Compartments 0 and 15 have only one neighboring compartment contributing to the axial current.

Table I gives the values and meanings of model parameters. Table II gives the details of the equations for the gating variables. Note that the conductance measurements are expressed in the unit of mS/cm². Each dendrite compartment has a diameter of 5.2 μm and a length of 81.7 μm, giving an area of 1334.67 μm², and the soma has an approximate area of 1000 μm²[29]. As a result, the value of soma axial conductance ($g_{5,4}$, $g_{5,6}$) is not equivalent with the value of dendrite axial conductance between soma and dendrite ($g_{4,5}$, $g_{6,5}$).

Ion concentrations dynamics. The outside space of the soma consists of an interstitial space and the bath, as shown in Fig. 1b. The concentrations for Na$^+$ and K$^+$ in the bath are always constant, while in the interstitial space and inside the soma ion concentrations they are variable and are closely related to neuron activities.

The ion concentrations are described by

$$\frac{d[\text{K}^+]_\text{o}}{dt} = J_{\text{Kcurrents}} - J_{\text{Kpump}} + J_{\text{Kglia}} - J_{\text{Kbath}} \qquad (6)$$

$$\frac{d[\text{K}^+]_\text{i}}{dt} = r_v \left(-J_{\text{Kcurrents}} + J_{\text{Kpump}} \right) \qquad (7)$$

$$\frac{d[\text{Na}^+]_\text{o}}{dt} = J_{\text{Nacurrents}} + J_{\text{Napump}} + J_{\text{Nabath}} \qquad (8)$$

$$\frac{d[\text{Na}^+]_\text{i}}{dt} = r_v \left(-J_{\text{Nacurrents}} - J_{\text{Napump}} \right), \qquad (9)$$

where the factor r_v corrects for the volume fraction between the interior of the cell and the interstitial space. For each item, $J_{\text{Kcurrents}}$ ($J_{\text{Nacurrents}}$) denotes ion fluxes caused by potassium currents I_K (sodium currents I_{Na}), J_{Kpump} (J_{Napump}) activity of the pump exchanging K$^+$ and Na$^+$, J_{Kglia} glial buffering, and J_{Kbath} (J_{Nabath}) diffusion of potassium (sodium) between the interstitial space and the bath. The expressions for the fluxes are given by

$$J_{\text{Kcurrents}} = \frac{I_\text{K} \times \text{A} \times 10^{-3}}{\text{F} \times \text{Volume}_{\text{shell}}}$$

$$J_{\text{Kpump}} = \frac{2 \times I_{\text{pump}} \times \text{A} \times 10^{-3}}{\text{F} \times \text{Volume}_{\text{shell}}}$$

$$J_{\text{Kglia}} = r_\text{b} \times ([\text{B}]_{\text{max}} - [\text{B}]) - r_\text{f} \times [\text{K}^+]_\text{o} \times [\text{B}]$$

$$J_{\text{Kbath}} = \frac{([\text{K}^+]_\text{o} - [\text{K}^+]_{\text{bath}})}{\tau_{\text{Kbs}}} \qquad (10)$$

$$J_{\text{Nacurrents}} = \frac{I_{\text{Na}} \times \text{A} \times 10^{-3}}{\text{F} \times \text{Volume}_{\text{shell}}}$$

$$J_{\text{Napump}} = \frac{3 \times I_{\text{pump}} \times \text{A} \times 10^{-3}}{\text{F} \times \text{Volume}_{\text{shell}}}$$

$$J_{\text{Nabath}} = \frac{([\text{Na}^+]_\text{o} - [\text{Na}^+]_{\text{bath}})}{\tau_{\text{Nabs}}}$$

For the glial uptake system, we adopt a phenomenological model where potassium homeostasis in the interstitial space is controlled by a buffering scheme and the free buffer concentration [B] is modeled by[47]

$$\frac{d[\text{B}]}{dt} = r_\text{b} \times ([\text{B}]_{\text{max}} - [\text{B}]) - r_\text{f} \times [\text{K}^+]_\text{o} \times [\text{B}], \qquad (11)$$

where

$$r_\text{f} = \frac{r_{\text{f0}}}{1 + \exp\left(\dfrac{[\text{K}^+]_\text{o} - [\text{K}^+]_{\text{th}}}{-1.15}\right)}.$$

3

Table I | Parameter values

R	Radius of soma	8.9×10^{-4} cm	(a)
F	Faraday's constant	96485 C/mol	(b)
τ_{Kbs}	K$^+$ diffusion time constant	500 ms	(c)
τ_{Nabs}	Na$^+$ diffusion time constant	$1.474\tau_{Kbs}$	(c)
Volume$_{shell}$	Volume of the interstitial space around soma	$4\pi R^3/3$	(b)
Volume$_{cell}$	Volume of soma	$4\pi R^3 r_v/3$	(b)
r_v	$r_v = \dfrac{\text{Volume}_{shell}}{\text{Volume}_{cell}}$	0.15	(d)
C_s	Soma capacitance	1.0 μF/cm^2	(d)
g_{NaF}	Fast Na$^+$ conductance	20.0 mS/cm^2	(e)
g_{NaP}	Persistent Na$^+$ conductance	0.24 mS/cm^2	(d)
g_{KDR}	Delayed-rectifier K$^+$ conductance	22.0 mS/cm^2	(e)
g_{KA}	A-type transient K$^+$ conductance	3.0 mS/cm^2	(d)
g_{KM}	Muscarinic K$^+$ conductance	3.0 mS/cm^2	(d)
g_{sLeak}	Soma leakage conductance	0.05 mS/cm^2	(c)
g_{KLeak}	Soma K$^+$ leakage conductance	0.154 mS/cm^2	(c)
g_{NaLeak}	Soma Na$^+$ leakage conductance	0.114 mS/cm^2	(c)
$g_{5,4}, g_{5,6}$	Soma axial conductance	7.35 mS/cm^2	(a, c)
E_{sLeak}	Soma leakage reversal potential	-60.0 mV	(c)
I_{max}	Pump maximal current	70.0 μA/cm^2	(c)
$[K^+]_{bath}$	Potassium concentration in the bath	7 mM	(e)
$[Na^+]_{bath}$	Sodium concentration in the bath	144 mM	(e)
$[B]_{max}$	Maximal buffer capacity	265 mM	(d)
r_b	Backward rate of buffer mechanism	0.0008/ms	(d)
r_{f0}	Equilibrium forward rate of buffer mechanism	0.0008 (mMms)$^{-1}$	(d)
$[K^+]_{th}$	Threshold $[K^+]_o$ for glia buffer	15 mM	(d)
C_d	Dendrite capacitance	1.88 μF/cm^2	(d)
$g_{4,5}, g_{6,5}$	Dendrite axial conductance between soma and dendrite	5.51 mS/cm^2	(a, c)
$g_{n \pm 1,n}$	Dendrite axial conductance between dendritic compartments ($n, n \pm 1 \neq 5$)	3.67 mS/cm^2	(d)
g_{dLeak}	Dendrite leakage conductance	0.0292 mS/cm^2	(d)
E_{dLeak}	Dendrite leakage reversal potential	-60.0 mV	(c)
A	LFS amplitude	1 μA/cm^2	(c)
ω	LFS angular frequency	0.002/ms	(c)
B	HFS amplitude	0–30 μA/cm^2	(c)
N	Ratio between the frequencies of LFS and HFS	$10^{0-1.8}$	(c)
ω'	HFS angular frequency	$N\omega$	(c)

Source: (a) Shuai *et al.*[29]; (b) definition; (c) estimated and/or modified values; (d) Park and Durand[30]; and (e) Park *et al.*[51].

Table II | Kinetics for gating variables

$$\frac{dm}{dt} = \frac{11.7 \times (11.5 - V_s)}{\exp\left(\frac{11.5 - V_s}{13.7}\right) - 1.0}(1.0 - m) - \frac{0.4 \times (V_s - 10.5)}{\exp\left(\frac{V_s - 10.5}{4.2}\right) - 1.0}m \qquad \text{(a)}$$

$$\frac{dh}{dt} = \frac{0.67}{\exp\left(\frac{V_s + 50.0}{5.5}\right)}(1.0 - h) - \frac{2.24}{\exp\left(\frac{72.0 - V_s}{29.0}\right) + 1.0}h \qquad \text{(a)}$$

$$\frac{dw}{dt} = \frac{\frac{0.07}{\exp\left(\frac{-V_s - 50.0}{2.0}\right) + 1.0} - w}{0.2} \qquad \text{(a)}$$

$$\frac{dn}{dt} = \frac{0.00049 \times V_s}{1.0 - \exp\left(\frac{-V_s}{25.0}\right)}(1.0 - n) - \frac{0.00008 \times (V_s - 10.0)}{\exp\left(\frac{V_s - 10.0}{10.0}\right) - 1.0}n \qquad \text{(a)}$$

$$\frac{da}{dt} = \frac{0.0224 \times (V_s + 30.0)}{1.0 - \exp\left(\frac{-V_s - 30.0}{15.0}\right)}(1.0 - a) - \frac{0.056 \times (V_s + 9.0)}{\exp\left(\frac{V_s + 9.0}{8.0}\right) - 1.0}a \qquad \text{(a)}$$

$$\frac{db}{dt} = \frac{0.0125}{\exp\left(\frac{V_s + 8.0}{14.5}\right)}(1.0 - b) - \frac{0.094}{\exp\left(\frac{-V_s - 63.0}{16.0}\right) + 1.0}b \qquad \text{(a)}$$

$$\frac{du}{dt} = 0.0084 \times \exp\left(\frac{V_s + 26.0}{40.0}\right)(1.0 - u) - \frac{0.0084}{\exp\left(\frac{V_s + 26.0}{61.0}\right)}u \qquad \text{(a)}$$
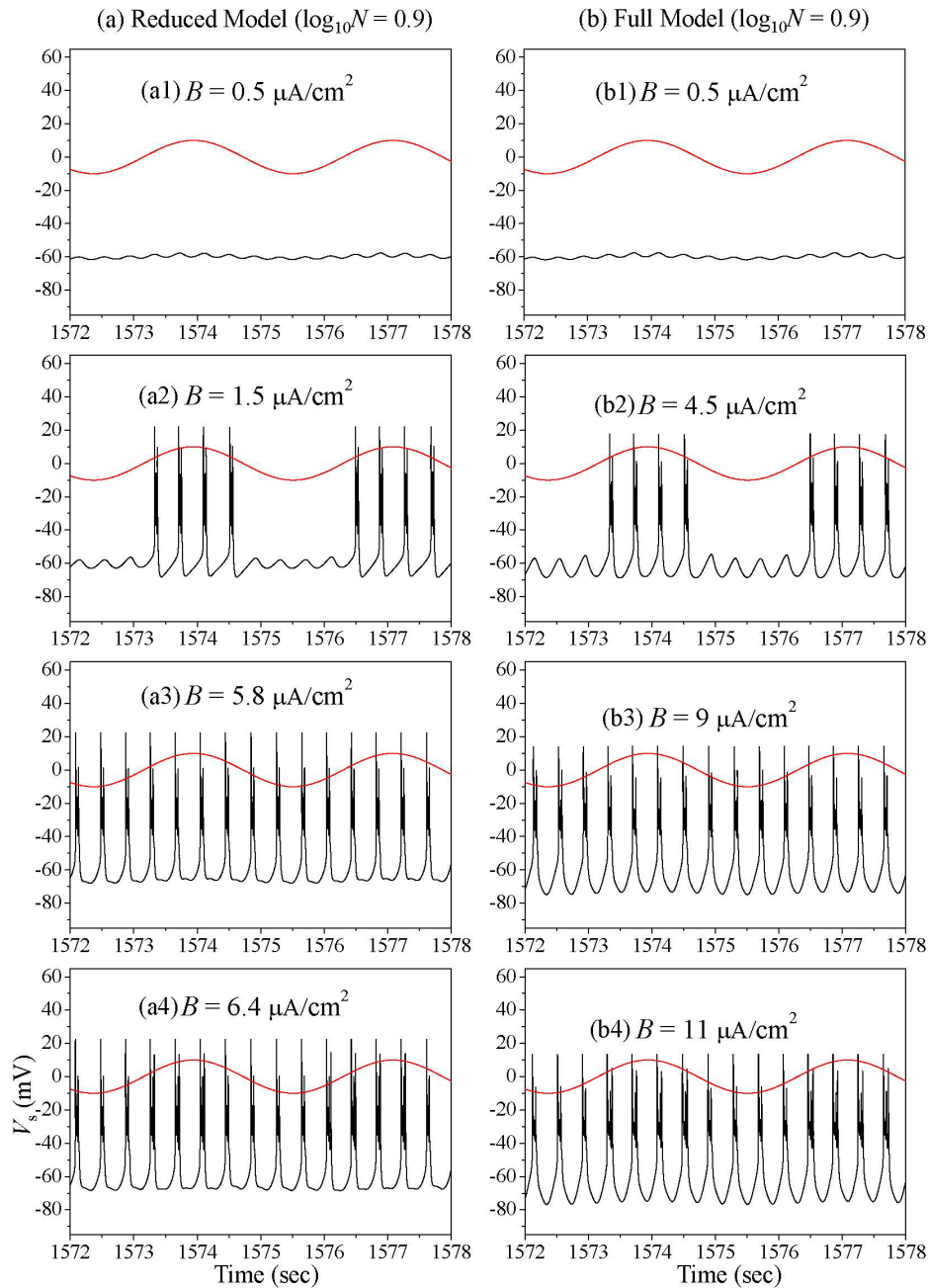
Source: (a) Park and Durand[30].

Figure 2 | Time evolutions of system output V_s for different HFS amplitudes B for the reduced model (a) and the full model (b). The red line in each panel represents a harmonic signal which has a higher amplitude than the LFS input. With the same evolving pattern, this new signal is adopted to more clearly observe the coherence between the LFS and the system output. For the LFS: $A = 1$ $\mu A/cm^2$ and $\omega = 0.002/ms$; and for the HFS: $B = 0.5$–11 $\mu A/cm^2$ and $\omega' = 10^{0.9} \omega$.

Reduced model. In order to show the contribution of the ion concentration dynamics to the detection of LFS, we formulate a reduction by fixing ion concentrations at their equilibrium values to make a comparison with the full model where the intra- and extracellular ion concentrations are dynamical variables rather fixed parameters. Resting ion concentrations are set as $[Na^+]_o = 144$ mM $[Na^+]_i = 15$ mM, $[K^+]_o = 7$ mM, and $[K^+]_i = 140$ mM. Thus, the reduced model is given by Eqs. (1)–(5) with constant resting ion concentrations.

Response to LFS. In order to discuss the system's VR response to LFS, the following responding factors have been defined[15]:

$$Q = \sqrt{Q_s^2 + Q_c^2}$$

$$Q_s = \frac{1}{T_2 - T_1} \int_{T_1}^{T_2} 2V_s(t)\sin(\omega t)dt$$

$$Q_c = \frac{1}{T_2 - T_1} \int_{T_1}^{T_2} 2V_s(t)\cos(\omega t)dt,$$

(12)

where T_1 is chosen sufficiently large in order to discard transient processing and $T_2 = T_1 + \frac{2n\pi}{\omega}$ where $n = 500$ unless otherwise specified. As information is carried through large spikes instead of
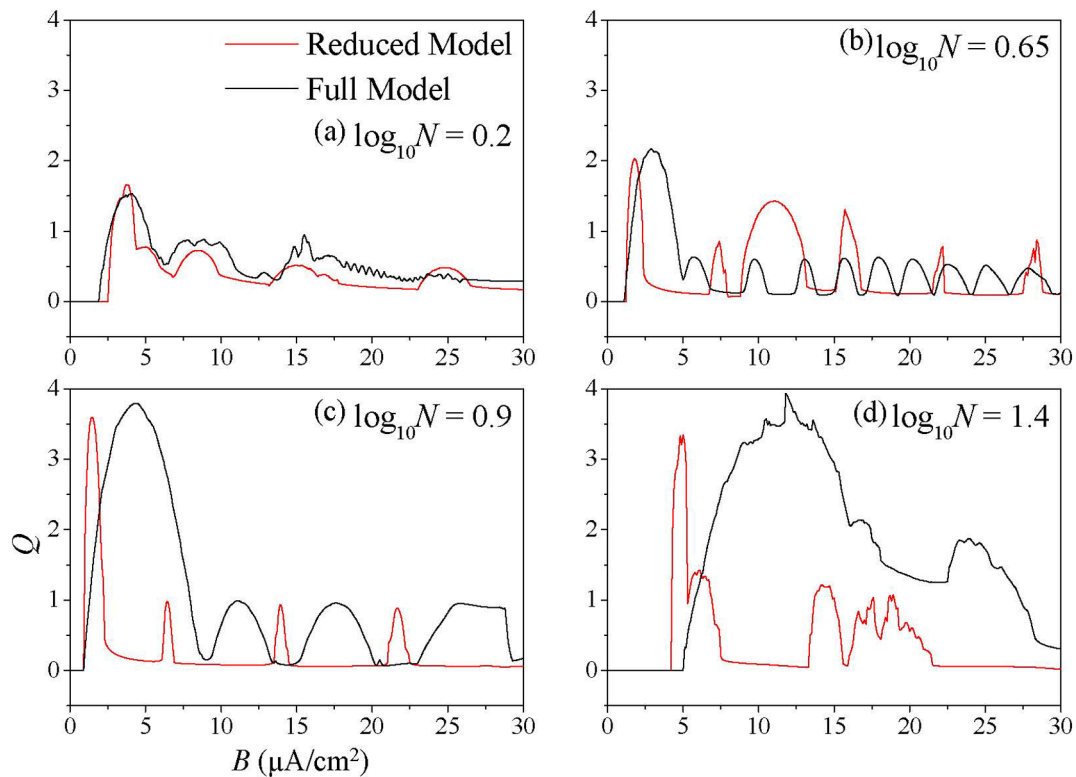
5

Figure 3 | Dependence of response Q as a function of B for different HFS frequencies. The difference between the results of the two models (red lines, reduced model; black lines, full model) reveals the role of ion concentrations dynamics in the production of multiple VR. For the LFS: $A = 1$ μA/cm^2 and $\omega = 0.002$/ms; and for the HFS: $B = 0$–30 μA/cm^2 and $\omega' = 10^{0.2, 0.65, 0.9, 1.4}$ ω.

subthreshold oscillations, we set a threshold $V_{\text{thre}} = -50.0$ mV to calculate Q. If $V_s < V_{\text{thre}}$, $V_s = -60$ mV; otherwise, V_s remains the same.

Results

Multiple VR enhanced by dynamical ion concentrations. The neuron is stimulated by two-frequency signals: a LFS and a high-frequency driving force. According to the definition of VR, we fix LFS component and observe the relation between the system output and the low-frequency signal with different amplitudes of the high-frequency driving force. Results for the full model and the reduced model under the same conditions are discussed and compared.

Fig. 2 depicts the time series of the somatic membrane potential V_s with respect to several particular amplitudes of the high frequency driving force for the reduced model (Fig. 2(a)) and the full model (Fig. 2(b)). LFS is periodic and subthreshold, as represented by red lines in each panel of Fig. 2, for the purpose of observing its coherence with the system output V_s (black lines). With the increase of amplitude of HFS, the system response to LFS varies in a similar fashion for these two models. When the amplitude of the high-frequency force is low ($B = 0.5$ μA/cm^2 for both models, Fig. 2(a1, b1)), it is noted that the neuron does not fire action potentials but only exhibits subthreshold oscillations around the resting potential.

By increasing the amplitude of the high frequency signel, spikes start to appear. At $B = 1.5$ μA/cm^2 for the reduced model (Fig. 2a2) and $B = 4.5$ μA/cm^2 for the full model (Fig. 2b2), during the positive half of LFS the neuron fires action potentials continuously while the outputs of neuron fluctuate slightly around the resting potential during the negative half part. Such responses are optimal ones where the firing is the most coherent with the low-frequency input.

With a further increase of the high frequency driving amplitude, it can be seen that the neuron fires relatively indiscriminately during both the positive half and the negative half of LFS (Figs. 2(a3, b3)). In

Figs. 2(a4, b4) with a higher amplitude, it is notable that the neuron's outputs have more spikes for each burst during the positive half than the negative half of the drive cycle of the low-frequency signal. Hence the synchronization between LFS and the neuron's outputs is slightly upgraded again. Therefore, the weak LFS is better transmitted at $B = 1.5$ μA/cm^2 and $B = 6.4$ μA/cm^2 for the reduced model and $B = 4.5$ μA/cm^2 and $B = 11$ μA/cm^2 for the full model.

According to Yang et al., the occurrence of VR can be induced by the transition between different phase-locking modes[52]. When driven only by the high-frequency force, the neuron displays either a non-firing state or a particular regular firing state depending on the intensity of the high-frequency force. The addition of a low frequency input will greatly change the neuron's output in some conditions during which a transition between different electrical states occurs repeatedly over time. For some amplitude values of HFS, the output of the system shows great synchronization with LFS with such a transition (Figs. 2(a2, a4; b2, b4)). For other values, however, little input/output synchronization is achieved without such a transition (Figs. 2(a1, a3; b1, b3)).

To measure the level of this synchronization, the factor Q is introduced. Fig. 3 depicts the response of Q to the LFS as a function of the high frequency amplitude for the two models. A higher value of Q indicates a higher coherence level between the neuron output and LFS, suggesting that LFS has been better transmitted to the neuron output through VR effect. The factor Q against the HFS amplitude for both models displays several peaks, indicating the occurrence of multiple VRs.

Irrespective of ion concentrations dynamics, multiple VRs occur commonly. The system has two input signals. The low frequency signal is fixed, while the HFS intensity is gradually increased. At first, the system does not exhibit any spike with low HFS amplitudes. Hence, the response Q is fixed at zero. Later, after increasing HFS intensity over a threshold, the system starts to fire spikes during the positive half cycle of the LFS, the number of which is directly associated with the value of Q. The response Q reaches its maximum immediately before the point when the negative half cycle of the
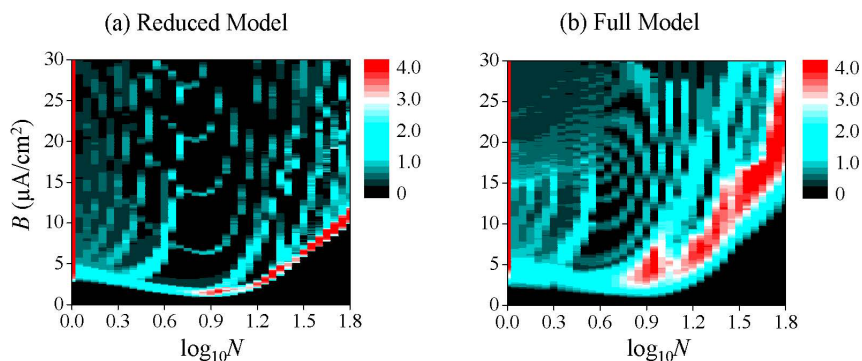
Figure 4 | **Contour plots of the response Q vs B and $\log_{10}N$ for the reduced model (a) and the full model (b).** The colors of black, cyan, and red correspond to increasing coherence levels. The role of ion concentrations dynamics in the production of multiple VR is better revealed by comparing these two figures. For the LFS: $A = 1$ $\mu A/cm^2$ and $\omega = 0.002/ms$; and for the HFS: $B = 0$–30 $\mu A/cm^2$ and $\omega' = 10^{0-1.8}$ ω.

LFS starts to have spikes. This is the peak of the first VR. Further increasing the HFS amplitude decreases the input-output coherence level. The second VR occurs when the spiking starts to get intensified during the LFS positive half cycle and so on for other VRs. The factor Q measures the difference between the spiking intensity in the positive and negative cycles of the LFS. Our simulation shows that the first VR typically has a highest value, indicating a largest difference of firing intensity in the two cycles of the LFS.

When the frequencies of the two input signals are around the same level (Fig. 3(a)), the two systems display VRs with similar widths. As the difference between the frequencies of these two signals is increased (Fig. 3(b)), the width of the first VR peak becomes obviously wider for the full model than for the reduced model. For the HFS with a much higher frequency (Figs. 3(c, d)), the full model leads to VRs with much wider peaks. Therefore, dynamical ion concentrations can cause the enlargement of the ranges of suitable high frequency driving levels, when the HFS has much higher frequency than the LFS. We will further test this conclusion from a more global view.

VR response against amplitude and frequency of HFS. To get a global view, the dependences of VR factor Q on the amplitude B of HFS and the frequency ratio $\log_{10}N$ are shown for both the reduced model (Fig. 4a) and the full model (Fig. 4b). The colors of black, cyan, and red correspond to increasing input-output coherence levels. The cyan and red areas represent the occurrence of VR.

Some VR features are independent of the ion concentrations dynamics, which could be revealed by the similarities of these two figures. First of all, the distribution of the cyan and red regions separated by black regions denotes the multiple VRs which occur for a wide choice of parameter sets. Secondly, the first VRs, corresponding to higher HFS frequencies, obviously correspond to higher Q values than other VRs. Finally, at $\log_{10}N = 0$ (i.e. $N = 1$), the two same input signals produce a strong resonance which is a special case called frequency-resonance-enhanced VR[53].

On the other hand, the difference of the two panels in Fig. 4 shows the role played by ion concentrations dynamics in signal transition. When the frequency difference between HFS and LFS is low, the VRs presented by the two models are not qualitatively differently. But approximately after $\log_{10}N > 0.9$, both the red areas and the cyan areas become much larger in Fig. 4b than in Fig. 4a. Especially, the band of the red areas which correspond to the first VR is obviously wider in the HFS amplitude for the full model than for the reduced model. Furthermore, this red region of the first VR locates differently and has a different slope for the two figures. This means that the first VR corresponds to a higher HFS amplitude for high HFS frequencies due to the ion concentrations dynamics and that ion concentrations dynamics elevates the HFS amplitude for the optimal coherence more

with the increase of the HFS frequency. Therefore, the dynamically evolving ion concentrations enhance VRs, including the first VR, when the HFS has a much higher frequency than the LFS. However, they also require more input energy (i.e. a higher amplitude) from the HFS in order to produce the maximal Q in the first VR.

VR response against amplitude of LFS. In addition, we investigate the multiple VRs responding to varying LFS amplitudes. Each panel in Fig. 5 depicts the dependence of factor Q on the HFS amplitude for several LFS amplitudes with differently colored lines. Three particular HFS frequencies have been chosen for the two models. The phenomenon of multiple VRs is observed for various LFS amplitudes. We notice some effects of the variation in the LFS amplitude on the multiple VRs.

First, there is a positive relation between the LFS amplitude and VRs. Many centers or the maximum points of VR peaks stay the same or shift a little bit for the varying LFS amplitude, compared to the distance of two nearby VR peaks along the HFS amplitude axis. With the increase of the LFS amplitude, the height and width of any VR tend to become larger. However, this influence may be barely distinguishable in some cases. For example, the first VRs almost have the same height for the four various LFS amplitudes in Fig. 5a1. We also notice that some small VR peaks melt away and are replaced by bigger ones. In Fig. 5b2, for example, the first two VR peaks grow and then merge into a bigger peak with the increase of the LFS amplitude.

Overall, it can be seen that the increasing LFS amplitude plays the similar role in these six panels, which means that the enlargement of VRs by the increase of LFS amplitude is a common behavior and does not depend particularly on the full model or the reduced model.

Discussion
In conclusion, both the reduced model and the full model are constructed to investigate the role of the dynamical ion concentrations in the expression of a low frequency signal through the neuron output modulated by another high frequency driving force. The reduced model has fixed ion concentrations, which is common for many neuronal computational models, while the full model has dynamically evolving ion concentrations, which is more physiologically realistic. We study VR behaviors with these two models driven by two periodic signals (i.e. a HFS and a LFS). Independent of the ion concentrations dynamics, the multiple VRs can be observed by adjusting the amplitude of the high frequency force and can take place in a wide range of control parameter values of driving signals and thus should be a common phenomenon. The result caused by the implementation of ion concentrations dynamics is that the multiple VRs become much stronger when the HFS frequency is much higher
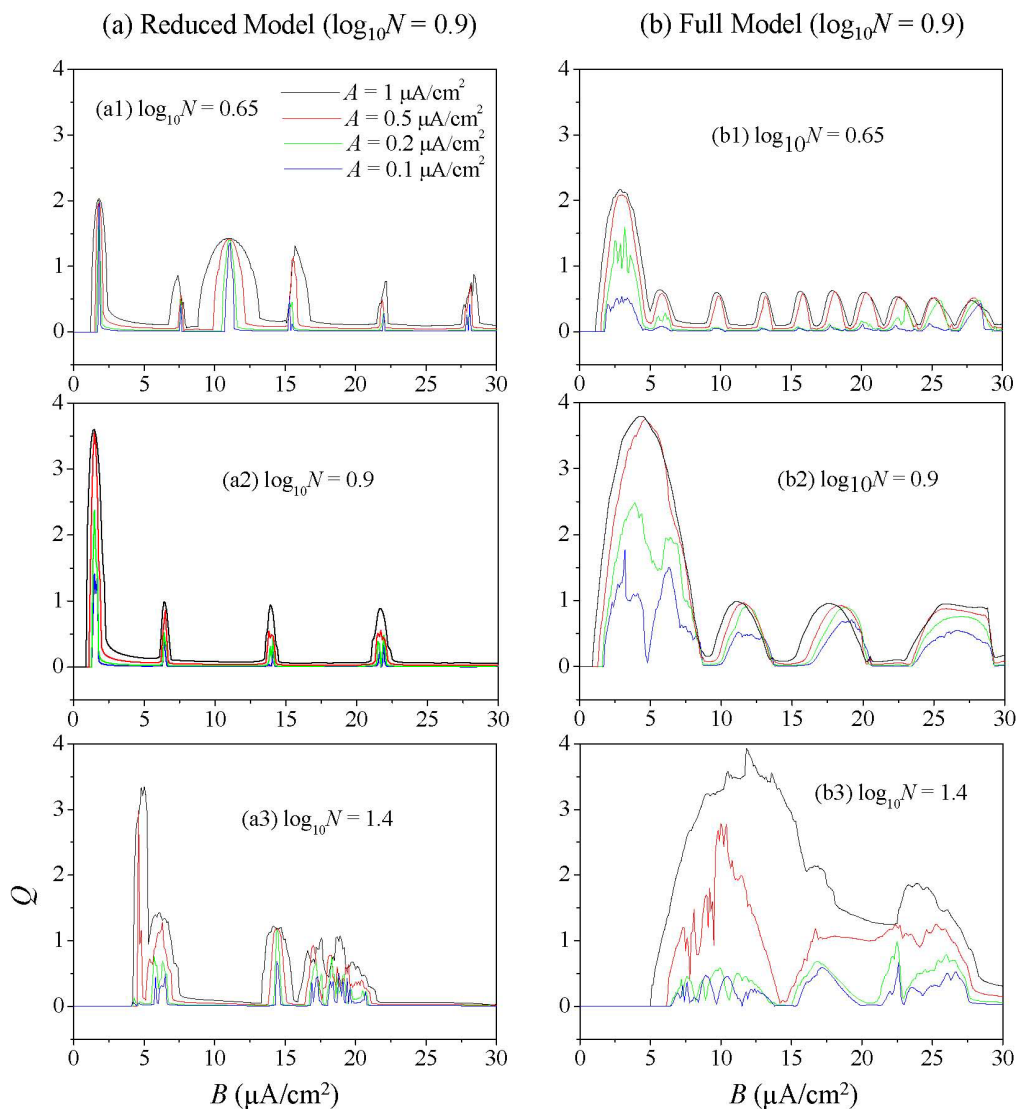
Figure 5 | Dependence of response Q as a function of B for different HFS frequencies for the reduced model (a) and the full model (b). In each panel, the differently coloured lines correspond to varying values of the intensity of LFS A. For the LFS: $A = 0.1–1$ $\mu A/cm^2$ and $\omega = 0.002/ms$; and for the HFS: $B = 0–30$ $\mu A/cm^2$ and $\omega' = 10^{0.65,0.9,1.4} \, \omega$.

than the LFS. Therefore, it is revealed that the neuron response to LFS can be largely enhanced by the ion concentrations dynamics.

It is normal in many computational simulations to fixate ion concentrations with the hypothesis that they would be restored to their equilibrium values immediately after neuronal activity. However, this point of view may seem extremely absurd as to signal detection for a biological neuron. Our simulations reveal a possible role played by the ion concentrations dynamics in a neuron: to enhance VRs when the high frequency driving force has a much higher frequency than the detected LFS, which may require more input energy (i.e. a high HFS amplitude) for the optimal first coherence in full model.

VRs are related to the spike number during the positive cycle of LFS relative to the spike number during the negative cycle. The more difference between the number of spikes during these two cycles, the better the coherence between the LFS and the neuron output. Generally, a higher HFS amplitude would cause more spikes during both the positive cycle and the negative cycle of LFS after when the stimulus is over a threshold (Fig. 2b in ref 50) but not with the same degree. During the negative cycle, however, no spike could be excited until the neuron gains enough input energy from the driving force to conquer the negative effect exerted by LFS, even when there are

already spikes during the positive cycle. The optimal coherence happens approximately at the point immediately before the generation of spikes during the negative cycle of LFS. The full model may stay non-firing during the negative cycle driven by a driving force with a particular amplitude around the optimal case, but this HFS amplitude can be strong enough to produce spikes during the negative cycle for the reduced model, because more input energy is required for the full model to push both membrane dynamics and ion concentrations dynamics to oscillate. This is consistent with the fact that the full model has a higher threshold of spiking in the intensity of a persistent DC current[50]. What happens is that, along with the increase of the HFS amplitude, ion concentration dynamics delay the occurrence of spikes during the negative cycle of LFS. Therefore, the optimal response of the neuron to LFS requires a higher amplitude of the driving force by the ion concentrations dynamics for the full model.

Secondly, ion concentrations dynamics cause VRs to have wider bell-like shapes. With a little increase in the HFS amplitude from the amplitude at the optimal VR, the number of spikes increases in the negative cycle of LFS. The variation in the number of spikes can be very different for the two models. For the reduced model, the

8

increment in the HFS amplitude may lead to almost the same spiking intensity during the negative and positive cycles. However, for the full model, the spikes during the negative cycle may be still much fewer than the ones during the positive cycle. The full model tends to change less in its behavior, responding to the same variation in the input signal. This is because ion concentrations tend to keep the neuron in its original state.

Many species of animals, such as weakly electric fish, have the ability to detect nearby objects by electric signals. They send out and accept signals with different frequencies. The principle of VR may be naturally applicable to carrier-based sensory neuronal systems, where the expression of LFS input becomes optimal. The single neuron model is able to extract low frequency stimulus from the modulated HFSs. Individual pyramidal cells in vitro have the ability to extract LFS, which strongly depends on intrinsic membrane noise[8]. We suggest that it could also depend on ion concentrations dynamics through the VR phenomenon.

In the model, the neuron consists of 16 compartments with 15 compartments for dendrites in order to simulate the dendritic structure of the neuron. Because only passive channels are assumed in the dendrite compartments and the active ion channels are only considered in soma, the dendrite structure actually plays little role in the behaviors discussed in the paper. We believe that a simplified model with only soma compartment will produce similar results. However, it would be more interesting to use a model with ion channels distributed along the dendrite structure. With such a model, one can investigate the effect of ionic fluxes in dendrites on signal detection.

1. Su, D., Chiu, M. & Chen, C. Simple two-frequency laser. *Prec. Eng.* **18**, 161–163 (1996).
2. Maksimov, A. On the subharmonic emission of gas bubbles under two-frequency excitation. *Ultrasonics* **35**, 79–86 (1997).
3. Victor, J. & Conte, M. Two-frequency analysis of interactions elicited by Vernier stimuli. *Visual Neurosci.* **17**, 959–973 (2000).
4. Gherm, V., Zernov, N., Lundborg, B. & Vastberg, A. The two-frequency coherence function for the fluctuating ionosphere: Narrowband pulse propagation. *J. Atmos. Sol. Terr. Phys.* **59**, 1831–1841 (1997).
5. Gherm, V., Zernov, N. & Lundborg, B. The two-frequency, two-time coherence function for the fluctuating ionosphere: wideband pulse propagation. *J. Atmos. Sol. Terr. Phys.* **59**, 1843–1854 (1997).
6. Heiligenberg, W. *Neural Nets in Electric Fish* [MIT Press] (Cambridge, MA, 1991).
7. Middleton, J., Longtin, A. J. B. & Maler, L. The cellular basis for parallel neural transmission of a high-frequency stimulus and its low-frequency envelope. *Proc. Natl. Acad. Sci. USA* **103**, 14596C14601 (2006).
8. Middleton, J. W., Girard, E. H., Maler, L. & Longtin, A. Envelope gating and noise shaping in populations of noisy neurons. *Phys. Rev. E* **75**, 021918 (2007).
9. Longtin, A., Middleton, J. W., Cieniak, J. & Maler, L. Neural dynamics of envelope coding. *Math. Biosci.* **214**, 87C99 (2008).
10. Kelly, N., Babineau, D. & Longtin, A. Electric field interactions in pairs of electric fish: modeling and mimicking naturalistic inputs. *Biol. Cybern.* **98**, 479C490 (2008).
11. McGillivray, P., Vonderschen, K., Fortune, E. & Chacron, M. J. Parallel Coding of First- and Second-Order Stimulus Attributes by Midbrain Electrosensory Neurons. *J. Neurosci.* **32**, 5510–5524 (2012).
12. Gerhardt, H. C. Significance of two frequency bands in long distance vocal communication in the green treefrog. *Nature* **261**, 692–694 (1976).
13. Han, J. S. Acupuncture: neuropeptide release produced by electrical stimulation of different frequencies. *Trends Neurosci.* **26**, 17–22 (2003).
14. Victor, J. & Conte, M. Two-frequency analysis of interactions elicited by Vernier stimuli. *Visual Neurosci.* **17**, 959–973 (2000).
15. Landa, P. & McClintock, P. Vibrational resonance. *J. Phys. A* **33**, L433–L438 (2000).
16. Gammaitoni, L., Hanggi, P., Jung, P. & Marchesoni, F. Stochastic resonance. *Rev. Mod. Phys.* **70**, 223–287 (1998).
17. Russell, D., Wilkens, L. & Moss, F. Use of behavioural stochastic resonance by paddle fish for feeding. *Nature* **402**, 291–294 (1999).
18. Jung, P. & Shuai, J. Optimal sizes of ion channel clusters. *Europhys. Lett.* **56**, 29–35 (2001).
19. Gitterman, M. Bistable oscillator driven by two periodic fields. *J. Phys. A* **34**, L355–L357 (2001).
20. Ullner, E., Zaikin, A., Garcia-Ojalvo, J., Bascones, R. & Kurths, J. Vibrational resonance and vibrational propagation in excitable systems. *Phys. Lett. A* **312**, 348–354 (2003).

21. Blekhman, I. & Landa, P. Conjugate resonances and bifurcations in nonlinear systems under biharmonical excitation. *Int. J. Non-Linear Mech.* **39**, 421–426 (2004).
22. Chizhevsky, V. N. & Giacomelli, G. Vibrational resonance and the detection of aperiodic binary signals. *Phys. Rev. E* **77**, 051126 (2008).
23. Jeyakumari, S., Chinnathambi, V., Rajasekar, S. & Sanjuan, M. A. F. Single and multiple vibrational resonance in a quintic oscillator with monostable potentials. *Phys. Rev. E* **80**, 046608 (2009).
24. Deng, B., Wang, J., Wei, X., Tsang, K. M. & Chan, W. L. Vibrational resonance in neuron populations. *Chaos* **20**, 013113 (2010).
25. Wickenbrock, A. *et al.* Vibrational Mechanics in an Optical Lattice: Controlling Transport via Potential Renormalization. *Phys. Rev. Lett.* **108**, 020603 (2012).
26. Yao, C. G. & Zhan, M. Signal transmission by vibrational resonance in one-way coupled bistable systems. *Phys. Rev. E* **81**, 061129 (2010).
27. Sun, J. *et al.* Vibrational resonance in neuron populations with hybrid synapses. *Appl. Math. Modell.* **37**, 6311–6324 (2013).
28. Xue, M., Wang, J., Deng, B. & Wei, X. Vibrational resonance in feedforward neuronal network with unreliable synapses. *Eur. Phys. J. B* **86**, 122 (2013).
29. Shuai, J., Bikson, M., Hahn, P. J., Lian, J. & Durand, D. M. Ionic mechanisms underlying spontaneous CA1 neuronal firing in Ca^{2+}-free solution. *Biophys. J.* **84**, 2099–2111 (2003).
30. Park, E.-H. & Durand, D. M. Role of potassium lateral diffusion in non-synaptic epilepsy: A computational study. *J. Theor. Biol.* **238**, 666–682 (2006).
31. Frankenhaeuser, B. & Hodgkin, A. L. The after-effects of impulses in the giant nerve fibres of Loligo. *J. Physiol.* **131**, 341–376 (1956).
32. Fertziger, A. P. & Ranck, J. B. Potassium accumulation in interstitial space during epileptiform seizures. *Exp. Neurol.* **26**, 571–585 (1970).
33. Heinemann, U., Lux, H. D. & Gutnick, M. J. Extracellular free calcium and potassium during paroxsmal activity in the cerebral cortex of the cat. *Exp. Brain Res.* **27**, 237–43 (1977).
34. Onizuka, S., Kasaba, T., Hamakawa, T., Ibusuki, S. & Takasaki, M. Lidocaine increases intracellular sodium concentration through voltage-dependent sodium channels in an identifed lymnaea neuron. *Anesthesiology* **101**, 110–119 (2004).
35. Raley-Susman, K. *et al.* Sodium influx blockade and hypoxic damage to CA1 pyramidal neurons in rat hippocampal slices. *J. Neurophysiol.* **86**, 2715–2726 (2001).
36. Muller, M. & Somjen, G. G. Na^+ and K^+ concentrations, extra- and intracellular voltages, and the effect of TTX in hypoxic rat hippocampal slices. *J. Neurophysiol.* **83**, 735–745 (2000).
37. Ekinci, E. I. *et al.* High sodium and low potassium intake in patients with Type 2 diabetes. *Diabet. Med.* **27**, 1401–1408 (2010).
38. Resnick, L. *et al.* Relation of cellular potassium to other mineral ions in hypertension and diabetes. *Hypertension* **38**, 709–712 (2001).
39. Zaza, A. Serum potassium and arrhythmias. *Europace* **11**, 421–422 (2009).
40. Ullah, G. & Schiff, S. J. Assimilating Seizure Dynamics. *PLoS Comput. Biol.* **5**, e1000776 (2010).
41. Anderson, W. R., Franck, J. E., Stahl, W. L. & Maki, A. A. Na,K-ATPase is decreased in hippocampus of kainate-lesioned rats. *Epilepsy Res.* **17**, 221–231 (1994).
42. Gabriel, S. *et al.* Effects of barium on stimulus induced changes in extracellular potassium concentration in area CA1 of hippocampal slices from normal and pilocarpine-treated epileptic rats. *Neurosci. Lett.* **242**, 9–12 (1998).
43. Feng, Z. & Durand, D. M. Effects of potassium concentration on firing patterns of low-calcium epileptiform activity in anesthetized rat hippocampus: Inducing of persistent spike activity. *Epilepsia* **47**, 727–736 (2006).
44. Amzica, F., Massimini, M. & Manfridi, A. Spatial buffering during slow and paroxysmal sleep oscillations in cortical networks of glial cells in vivo. *J. Neurosci.* **22**, 1042–1053 (2002).
45. Resnick, L. M. *et al.* Effects of potassium concentration on firing patterns of low-calcium epileptiform activity in anesthetized rat hippocampus: Inducing of persistent spike activity. *Epilepsia* **47**, 727–736 (2006).
46. Cressman, J. R., Ullah, G., Ziburkus, J., Schiff, S. J. & Barreto, E. The influence of sodium and potassium dynamics on excitability, seizures, and the stability of persistent states: I. Single neuron dynamics. *J. Comput. Neurosci.* **26**, 159–170 (2009).
47. Kager, H., Wadman, W. J. & Somjen, G. G. Simulated seizures and spreading depression in a neuron model incorporating interstitial space and ion concentrations. *J. Neurophysiol.* **84**, 495–512 (2000).
48. Barreto, E. & Cressman, J. R. Ion concentration dynamics as a mechanism for neuronal bursting. *J. Biol. Phys.* **37**, 361–373 (2011).
49. Bazhenov, M., Timofeev, I., Steriade, M. & Sejnowski, T. J. Potassium model for slow (2–3 hz) in vivo neocortical paroxysmal oscillations. *J. Neurophysiol.* **92**, 1116–1132 (2004).
50. Wu, X. X. & Shuai, J. W. Multistability in a neuron model with extracellular potassium dynamics. *Phys. Rev. E* **85**, 061911 (2012).
51. Park, E.-H., Feng, Z. & Durand, D. M. Diffusive coupling and network periodicity: A computational study. *Biophys. J.* **95**, 1126–1137 (2008).
52. Yang, L. *et al.* Vibrational resonance induced by transition of phase-locking modes in excitable systems. *Phys. Rev. E* **86**, 016209 (2012).
53. Yao, C., Liu, Y. & Zhan, M. Frequency-resonance-enhanced vibrational resonance in bistable systems. *Phys. Rev. E* **83**, 061122 (2011).

Acknowledgments

Author contributions

J.S. and C.Y. conceived the idea. J.S. directed the work. X.-X.W. performed the calculations and data analysis. All authors contributed to writing the manuscript.

Additional information

Competing financial interests: The authors declare no competing financial interests.

How to cite this article: Wu, X.-X., Yao, C. & Shuai, J. Enhanced multiple vibrational resonances by Na$^+$ and K$^+$ dynamics in a neuron model. *Sci. Rep.* **5**, 7684; DOI:10.1038/srep07684 (2015).